Contents lists available at ScienceDirect

Applied Catalysis B: Environmental

Reveal Brønsted–Evans–Polanyi relation and attack mechanisms of reactive oxygen species for photocatalytic H$_2$O$_2$ production

Jun Luo [a], Changzheng Fan [a,*], Lin Tang [a,*], Yani Liu [b], Zhixuan Gong [a], Tangshan Wu [a], Xinlan Zhen [a], Chengyang Feng [a], Haopeng Feng [a], Lingling Wang [c], Liang Xu [d], Ming Yan [a]

[a] College of Environmental Science and Engineering, Key Laboratory of Environmental Biology and Pollution Control (Ministry of Education), Hunan University, Changsha 410082, China
[b] Key Laboratory of Water Pollution Control Technology, Hunan Research Academy of Environmental Sciences, Changsha 410004, China
[c] Key Laboratory for Micro-Nano Physics and Technology of Hunan Province, School of Physics and Electronics, Hunan University, Changsha 410082, China
[d] Energy Materials Computing Center, Jiangxi University of Science and Technology, Nanchang 330013, China

ARTICLE INFO

ABSTRACT

The generation of H$^+$ by active species attacking proton donor (PD) is a key step in photocatalytic H$_2$O$_2$ production (PHP). Deeply analyzing the involved mechanism may be a crucial factor to break through the bottleneck of H$_2$O$_2$ yield. Here, nitrogen-deficient and boron-doped g-C$_3$N$_4$ are synthesized for PHP and the interaction mechanisms between active species and PD are revealed. The prepared photocatalyst exhibits a high H$_2$O$_2$ production rate (455 μM h^{-1} g^{-1}). The ^{1}O$_2$, •O$_2^-$ and hole promoted by modification site dominate twelve different reaction mechanisms, respectively. For the oxidation pathways dominated by hole, H$_2$O$_2$ generation is limited by the dissociation of PD or desorption of H$^+$ on catalyst surface. Interestingly, •O$_2^-$ and ^{1}O$_2$ could directly attack PD, or diffuse into solution to react with PD to produce H$_2$O$_2$ with lower barriers. Moreover, there is a synergistic effect between doped-boron, ^{1}O$_2$ and water bridge, which further reduces the reaction barrier.

1. Introduction

As a promising liquid fuel, hydrogen peroxide (H$_2$O$_2$) has received much attention as it is storable and transportable [1]. Photocatalytic H$_2$O$_2$ production (PHP) is a low-cost and environmentally friendly way and has been extensively studied [2–6]. But the sluggish oxidation of water results in extremely low yield of H$_2$O$_2$, which is difficult to meet the needs of practical applications [7]. In contrast, addition of proton donor (PD), such as isopropyl alcohol (IPA), benzyl alcohol (BA) and 2-PrOH, can significantly increase H$_2$O$_2$ yield [8–10] and has been successfully applied to disinfection of *Escherichia coli* [2]. Surprisingly, using benzylamine as PD, Han and co-workers not only prepared H$_2$O$_2$, but also obtained a value-added chemical, benzonitrile, which further demonstrated the huge potential of photoproduction of H$_2$O$_2$ with using PD in practical applications [11].

Currently, holes are recognized as the only driving force for the generation of hydrogen sources in H$_2$O$_2$. The generated H$^+$ undergoes the processes of anchoring on the photocatalyst surface and combining with the reduced O$_2$, i. e. the processes of H$^+$ adsorption and desorption. These processes are similar to the dissociation of N$_2$ and the desorption

of NH$_x$ in ammonia synthesis on catalyst surface, which is regulated by the Brønsted–Evans–Polanyi (BEP) relation [12,13]. That is, stronger adsorption of N atom suggests lower N$_2$ dissociation barrier but higher NH$_x$ desorption energies. For the recognized mechanism of PHP, the adsorption and desorption of H$^+$ may also follow a similar BEP relation (BEP-like relation), which may become a key factor restricting H$_2$O$_2$ generation like ammonia synthesis. Unfortunately, there is no report on the BEP-like relation in PHP. According to previous reports, the introduction of nitrogen vacancies (NV) lead to the generation of defective electronic states in graphitic carbon nitride (CN) [3], and the boron-doped downshifts the valence band (VB) of CN [14], which implies that the two modification sites have different abilities to oxidize PD. Therefore, it can be speculated that the CN modified by NV and boron-doped may be an ideal model for studying BEP-like relation in PHP.

In addition to holes, a variety of active oxygen species (ROS) are also generated during the photocatalytic process, such as hydroxyl radicals (•OH), superoxide radical anion (•O$_2^-$) and singlet oxygen (^{1}O$_2$). These ROS with oxidizing ability may also provide driving forces for the dissociation of proton donors and the generation of H$^+$. Therefore,

---

promoting the production of ROS may be an effective strategy to increase H_2O_2 yield. However, it is widely accepted that H_2O_2 is formed by the combination of ROS, such as $\bullet O_2^-$ [10] and $^1O_2$ [15], and H^+ generated by the oxidation of holes, and there is currently no research on the attack pathway of ROS on PD.

As mentioned above, NV site and boron-doped site have different effects on the electronic structure of CN, which may lead to different dissociation barriers of PD and promote the generation of different ROS. Thus, we synthesized nitrogen-deficient and boron-doped g-C_3N_4 (NBCN) and used it to firstly study the BEP-like relation and interaction mechanism between active species and PD in PHP. Through experiments and theoretical calculations, this work (i) explores the oxidation behaviors and limitations of the holes on photocatalyst surface to PD, (ii) discusses the promoting effects of the two modification sites on the generation of active species, and (iii) proposes 12 pathways for H_2O_2 generation, highlighting the direct attack of ROS on PD, and the indirect proton transfer with the assistance of water bridge. This study designs a promising photocatalyst for H_2O_2 evolution, proposes and verifies the BEP-like relation, and reveals the novel reaction mechanism related to ROS in PHP.

2. Experimental section

2.1. Synthesis of the catalysts

2.1.1. Synthesis of CN samples

For a typically preparation of pristine g-C_3N_4, 15 g melamine was calcined at 520 °C in a muffle furnace for 4 h with a heating rate of 10 °C min^{-1}.

2.1.2. Synthesis of CN samples

2 g of as-prepared CN and 0.8 g of $NaBH_4$ were ground and mixed fully. Then the mixture was calcined at different temperatures (350, 400, 450 ºC) under nitrogen atmosphere for 1 h with a heating rate of 5 ºC min^{-1}. The obtained samples were washed with water and alcohol for several times. The final products were denoted as NB-x, where x represents the calcining temperature.

2.2. Characterization

The phase structures of the samples were analyzed by X-ray diffraction (XRD) measurement on a Bruker D8 Advance instrument with Cu Kα radiation (λ = 0.15418 nm). The morphologies were collected on a FEI Quanta 250 scanning electron microscopy (SEM). The surface chemical compositions were studied by X-ray photoelectron spectroscopy (XPS, ESCALAB 250Xi, Thermo Fisher). The diffuse reflectance absorption spectra (DRS) of the samples were measured by a Varian Cary 300 spectrophotometer with $BaSO_4$ reference from 200 to 800 nm. The photoluminescence (PL) spectroscopy was monitored by a PerkinElmer LS-55 fluorescence spectrophotometer with an excitation wavelength of 350 nm at room temperature. FTIR was measured on an IR Prestige-21 spectrometer using samples embedded in potassium bromide (KBr) pellets. ESR spectra were measured on a JEOL JES-FA200 spectrometer at room temperature under visible light irradiation (λ > 420 nm). 5,5-dimethyl-L-pyrroline N-oxide (DMPO) was used as the trapping reagent for $\bullet O_2^-$ and $\bullet OH$. 2,2,6,6-tetramethylpiperidine (TEMP) was used as the trapping reagent for $^1O_2$.

2.3. Rotating ring-disk electrode (RRDE) measurements

RRDE measurements were performed through an electrochemical workstation (Chenhua CHI 760E). The ring potential of ring-disk electrode was sustained at 1.48 V (vs. RHE). The Ag/AgCl electrode and carbon rod were employed as the reference and counter electrode, respectively. The linear sweep voltammetry (LSV) curves were acquired in an O_2-saturated 0.10 M phosphate buffer solution. Prior to

measurements, 5.0 mg of prepared photocatalyst was dispersed in 1.0 mL of ethanol (with 0.05% Nafion) and ultrasonicated for 30 min. Then, 10 μL of the above suspension was dripped onto the glassy carbon disk and dried at room temperature. The number of the transferred electrons was calculated following equation:

$$n = 4 \frac{I_d}{I_d + I_r/N}$$

where I_d is the disk current, I_r is the ring current. The collection efficiency (N) is determined to be 37%.

2.4. Photocatalytic H_2O_2 production

100 mg of catalyst was uniformly dispersed into 100 mL of water or mixed solution containing 10 mL of isopropanol (IPA) and 90 mL of water with ultrasonication for 10 min. Then the suspension solutions were stirred for 30 min in the dark to reach the absorption-desorption equilibrium. The light source was provided by a 300 W xenon lamp (PLS-SXE300D/300DUV, Beijing Perfectlight) with 420 nm cutoff filter. The distance between the reactor and the light source was set as 15 cm, and the solution was kept stirring during the experiment at 25 °C. At certain time intervals, 3 mL suspension was sampled and centrifuged to remove the photocatalysts. The amount of H_2O_2 was measured by iodometry [16].

2.5. Computational details

Geometries and energies were carried out using the Perdew−Burke−Ernzerhof (PBE) functional [17] with the approach of Grimme (DFT-D3) [18] as implemented in the Vienna ab initio simulation package (VASP) [19]. The optimized lattice parameters were 16.73, 12.71, 15.00 Å, and 90.0, 90.0, 90.0º, respectively. Atomic positions were relaxed until the forces were less than 0.02 eV/Å. The projector augmented wave method (PAW) was used to describe the interaction between the ions and the electrons [20]. The energy cutoff of the plane wave was set to 600 eV. The Brillouin zone was sampled using a Gamma k-point of $3 \times 4 \times 1$. The VASPsol implicit solvation model was used to simulate the experimental solution environment [21]. The pre- and post-processings of the calculation were finished via the VASPKIT [22]. The DOS relative to the vacuum energy level can be obtained by extracting calculation data without shifting the Fermi energy level to zero [23]. The Fermi energy level was obtained from the self-consistent calculation of OURCAR.

Before performing TDDFT calculations, it is necessary to convert VASP-optimized geometry into cluster model with periodicity [24]. First, the periodicity of the VASP-optimized geometry was removed. Subsequently, hydrogen atoms were added to passivate the unsaturated N atoms located at the edges based on their original coordination. Then, only the hydrogen atoms used to passivate the boundary were optimized and other atoms were fixed. Finally, a cluster model with periodicity was obtained. TDDFT calculations at the cluster model with periodicity were carried out at the M062X-D3[25,26]/6–311 G(d,p) [27] level as implemented in Gaussian 16 C.01 code [28]. In order to be consistent with the experimental solution environment, self-consistent reaction field (SCRF) with the SMD model [29] were used and water was chosen as the solvent. The analysis of the excited state were finished via the Multiwfn 3.8(dev) code [30]. Most structure and isosurface maps were visualized by VMD [31].

The climbing-image nudged elastic band (CI-NEB) [32] and DIMER [33] methods as implemented in the CP2K/Quickstep package [34], were used to optimize the transition state and further confirmed by vibrational frequency analysis. To describe the aqueous environment more accurately, we include 58H_2O molecules on the VASP-optimized NBCN surface. In the calculation of reaction pathway, trapped holes and electrons were simulated by introducing OH group [35] and

potassium atom [36] into the system, respectively. CP2K/Quickstep employed a hybrid Gaussian and plane wave basis set and Goedecker-Teter-Hutter (GTH) pseudopotentials [37,38]. The plane wave cutoff was set to 500 Ry. The Gaussian basis set consisting of a double-ζ with one set of polarization functions (DZVP) [39] was used to optimize structures. For the energy calculation in reaction pathway, the triple-ζ with one set of polarization functions (TZVP) basis set was employed. The Perdew−Burke−Ernzerhof exchange-correlation functional [17] with the approach of Grimme (DFT-D3) [25] was adopted. Due to the large size of the model, single gamma point grid sampling was used. The free energy could be calculated as $\Delta G = \Delta E + \Delta E_{ZPE} - T\Delta S$, where ΔE is the reaction energy, ΔE_{ZPE} is the zero-point energy, T is temperature, and ΔS is entropy difference between the products and the reactants.

3. Results and discussion

3.1. Experimental characterization

The crystal structure of the samples were first characterized by X-ray diffraction (XRD) patterns. The XRD pattern of CN (Fig. S1a) shows two characteristic peaks at 13.0° and 27.4°, which can be assigned to the intralayer repeated packing heptazine units (100) and interlayer stacking (002) of graphitic CN, respectively [40]. For NB-*x* samples, a gradual weakening can be observed on both the two characteristic peaks with the increasing calcination temperature, indicating that the addition of NaBH₄ caused the loss of ordered structures within the framework. The Fourier transform infrared spectroscopy (FTIR) spectrum for CN (Fig. 1a) show a peak at 803 cm^{-1} originating from the out-of-plane bending mode of triazine unit. The peaks in the range of 1200–1700 cm^{-1} correspond to the stretching modes of aromatic C–N heterocycles. Multiple broad peaks locating between 3000 and 3500 cm^{-1} were typically for N-H stretching vibrations. A peak

originating from the cyano groups (–C≡N) emerged at 2168 cm^{-1} for NB-*x* suggesting that cyano groups [41] were introduced to the CN after adding NaBH₄.

The bulk element ratios of prepared samples were determined by organic elemental analysis (OEA) and inductively coupled plasma optical emission spectrometer (ICP-OES). As shown in Fig. S2, the N/C atomic ratios of NB-*x* slightly decreased with the increase of calcination temperature. Meanwhile, the B element content increased from 0% to 0.838%. These indicate that the addition of NaBH₄ leads to the reduction of N elements and the introduction of B elements in the bulk. The SEM images show that the NaBH₄ treatment did not significantly change the morphology of the samples (Fig. S3). N₂ adsorption–desorption measurements show that the BET specific surface area of CN and NB-*x* (*x* = 350, 400, 450) are 14.2588, 15.9159, 13.7189 and 16.7210 m² g^{-1}, respectively (Fig. S5a), indicating that NaBH₄ treatment has no obvious effect on the specific surface area of CN.

X-ray photoelectron spectroscopy (XPS) analysis was performed to further study the surface chemical state of the samples. The XPS survey spectra of CN and NB-*x* (Fig. S4) are basically the same, indicating that their surface elemental composition is similar. However, the narrow scan B 1s spectra (Fig. 1b) show that the intensity of B 1s peak increases and gradually shifts to higher binding energy with the increasing calcination temperature. As shown in Fig. 1c, the C1s XPS spectra of CN possesses three peaks of 288.11, 286.41, and 284.8 eV, corresponding to N-C=N, C-NH$_x$ (*x* = 1, 2) and adventitious hydrocarbons, respectively [42]. After NaBH₄ treatment, the intensity of C-NH$_x$ peak increases with the increasing calcination temperature. This also proves the introduction of C≡N, because the cyano group has similar binding energy [43]. In the N1s XPS spectra (Fig. 1d), three peaks at 398.59, 400.33, and 401.00 eV for CN refer to bi-coordinated N (N$_{2\,C}$), tri-coordinated N (N$_{3\,C}$), and N-H$_x$ groups in the heptazine framework, respectively [44]. With the increase of calcination temperature, the intensity of N$_{2\,C}$ in NB-*x* gradually decreases. Meanwhile, the intensity of N$_{3\,C}$ increases and
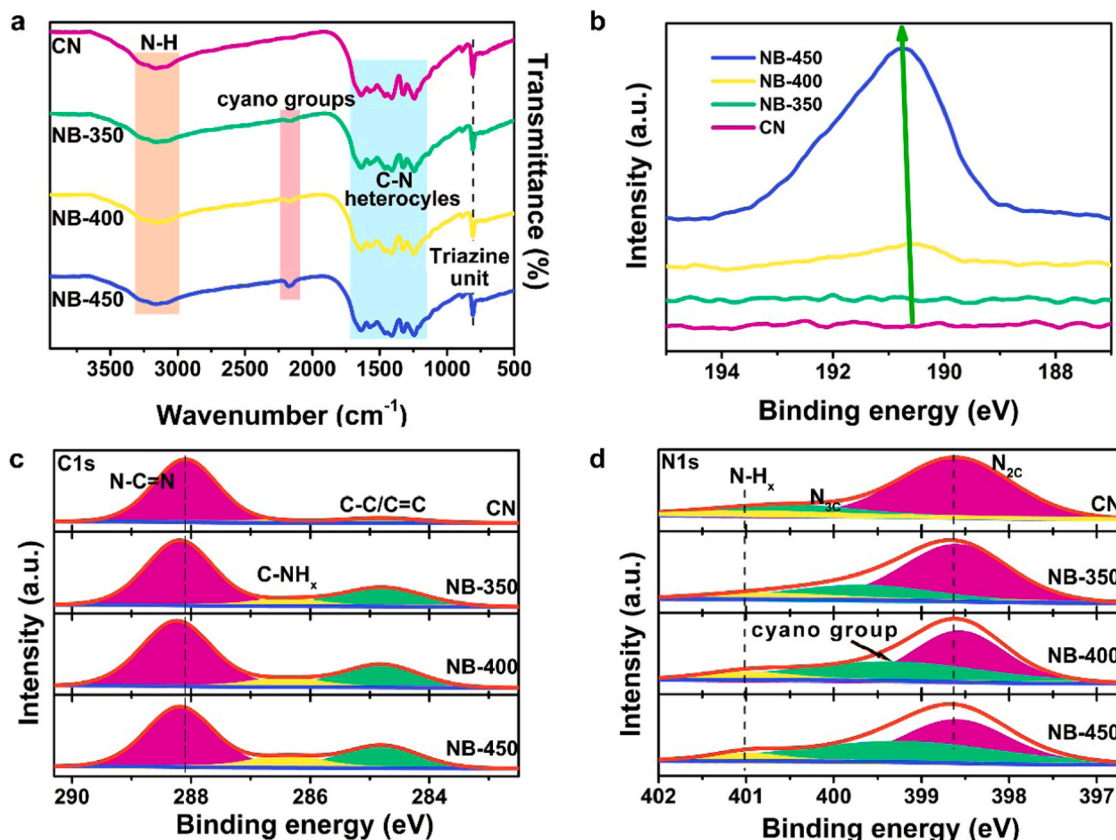

Fig. 1. (a) FTIR spectra of CN and NB-*x*. (b) B1s (c) C1s and (d) N1s XPS spectra of CN and NB-*x*.

the peak shifts to lower binding energy. These once again confirm the introduction of cyano groups, because their binding energy lies between those of N_{3C} and N_{2C} [43]. The surface atomic ratio of each element obtained by fitting XPS spectra was summarized in Fig. S6. The atomic ratio of N decreased from 54.25% to 42.17%, and that of B increased from 0% to 2.95%. In contrast, the small increase in the atomic ratio of C can be attributed to the substantial decrease in the counterpart of N. Based on the above analysis, it can be speculated that there are a large number of N defects on the surface. Meanwhile, since the decreases of N are much greater than the increases of B, it can be reasonably speculated that the introduced B atoms were more likely to replace the N atoms in the melon unit. To determine the specific sites of NV and B doping, the specific atomic ratios of nitrogen in N-H_x, N_{3C} and N_{2C} based on XPS data were summarized in Fig. S7. It can be observed that the decrease of N element is mainly due to the decrease of N_{2C} content. Therefore, NV and B doping sites can be determined on the N_{2C} sites.

The doped B lead to redistribution of electron density in the heptazine framework. With the increase of B doping, the N 1s peaks exhibit a shift to lower binding energy (Fig. 1d), while the B 1s and C 1s peaks shift to higher binding energy, respectively (Fig. 1c,d). This suggests that the electron density of N increases and the electron density of C and B decrease after B was introduced. The above phenomenon can be explained as follows: (1) When the N at the N_{2C} site is replaced by B, the electrons in B tend to transfer to the adjacent N, because the electronegativity of N and B are the strongest and weakest in NBCN, respectively; (2) Since B has fewer valence electrons compared to the replaced N, it provides fewer electrons to form the B-C covalent bond, resulting in a decrease in the electron density of C; (3) Furthermore, the affected C are more likely to be close to the neighboring N to obtain shared

electrons. Even so, since the electronegativity of N is stronger than that of C, the share electron pair between them is biased toward N to prevent the electron density of C from increasing, which also leads to an increase in the electron density of N. On the other hand, the above analysis can be mutually verified with DFT calculation. As shown in Fig. S8, the original distance between N1 and N2 is 2.68 Å. After N2 is replaced by B1, the distance between N1 and B1 is reduced to 2.66 Å, indicating that there is a stronger electron transfer between N1 and B1 than before. The C1-N2 bond length increased from 1.33 to 1.45 Å (C1-B1), implying that the covalent strength of C1-B1 was weaker than before doping. The C2-B1 bond has the same trend. C1 with reduced shared electrons tends to be closer to N4 because the corresponding bond length is reduced from 1.38 to 1.36 Å. The above calculation results are completely consistent with the experimental conclusions.

The optical properties of the samples were characterized by UV–vis diffuse reflectance spectroscopy (DRS). Compared with CN, the NaBH4 treatment resulted in a gradual red shift of the absorption edge for samples (Fig. 2a), and the bandgap narrowed from 2.59 to 2.20 eV (Fig. 2b). As determined from the VB XPS spectra, the VB potential for CN and NB-x ($x = 350, 400, 450$) samples are located at about 2.05, 2.19, 2.29 and 2.34 eV, respectively (Fig. 2c). The VB maximum (VBM) of CN and NB-x ($x = 350, 400, 450$) samples are calculated to be 1.49, 1.62, 1.72 and 1.77 eV (vs NHE) by the following equation $E_v = \Phi + VB_{max} - 4.44$ [45], where Φ is the electron work function of the analyzer (3.88 eV) and VB_{max} is the VB potential. Based on the above data, the conduction band minimum (CBM) can be calculated. As shown in Fig. 2d, after adding NaBH4, both CB and VB downshift to more positive potentials and CB exhibits a greater magnitude of downward shift, resulting in reduction of bandgap.
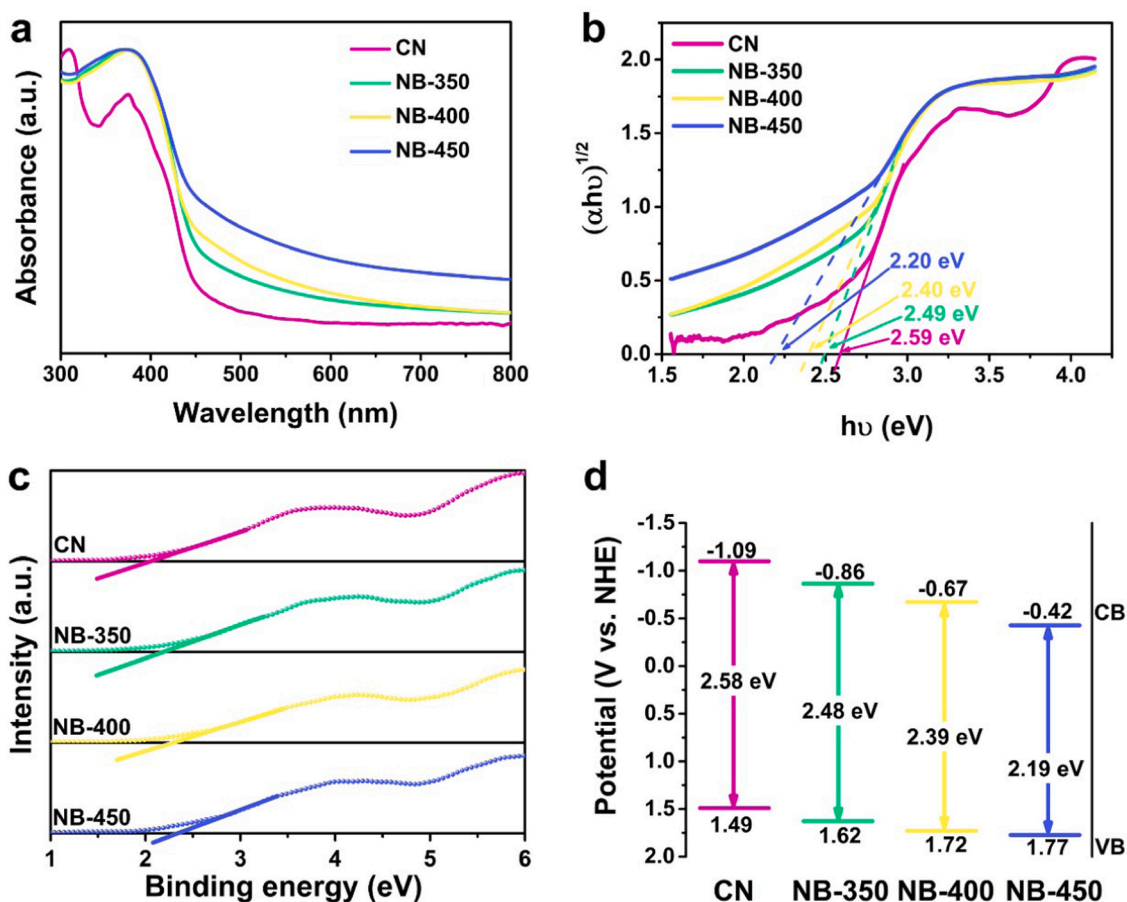

Fig. 2. (a) UV–vis DRS and (b) plots of transformed Kubelka–Munk function versus photon energy of CN and NB-*x*. (c) VB XPS spectra of CN and NB-*x*. (d) The band structure alignments of CN and NB-*x*.

3.2. Evaluation of PHP performance

The performances for PHP were evaluated in an O_2-equilibrated condition under visible light ($\lambda \geq 420$ nm) irradiation in the presence of IPA. As shown in Fig. 3a, the CN exhibits a H_2O_2 production rate of 59 µM h^{-1}. Interestingly, the H_2O_2 productive rate of NB-x ($x = 350$, 400 and 450) samples significantly increased to 362, 455 and 405 µM h^{-1}, respectively. NB-400 samples show the best performance for PHP, which is 7.7 times higher than that of the CN. In addition, no H_2 was produced during the photocatalysis process (Fig. S9). This is mainly because electrons are captured by O_2 under O_2-saturated conditions, so they cannot combine with protons to produce H_2 [46]. Photoluminescence (PL) spectroscopy measurements were performed to explore the charge transfer dynamics of samples. As shown in Fig. 3b, there is a strong PL signal centered at 466 nm for CN. In contrast, the PL intensity of NB-x gradually decreases with increasing calcination temperature, indicating that the intrinsic radiative recombination of photogenerated charge carrier is suppressed under the coordinated modification of nitrogen defects and boron doping [47]. Photocatalytic reduction of oxygen to H_2O_2 is a typical two-electron transfer process and there may be side reactions of four-electron and single-electron transfer. Therefore, the average electron transfer numbers (n) in the photocatalytic reaction is a vital index to determine the selectivity of PHP. Fig. 3c depicts the measured disk and ring currents of NB-400 and CN on a rotating ring-disk electrode (RRDE), respectively. The n on NB-400 and CN electrodes were calculated as 2.38 and 2.86, respectively (Fig. 3d), indicating that NB-400 is more selective for the PHP compared to CN.

3.3. Experimental research on reaction mechanism

To reveal the mechanism of PHP, electron spin resonance (ESR) technology was first performed to confirm the existence of $\bullet O_2^-$ and $^1O_2$. As shown in Fig. 4a,b, NB-400 shows stronger $\bullet O_2^-$ and $^1O_2$ signals compared to the counterparts of CN under light irradiation. It is worth mentioning that the VBM of NB-400 (+1.72 V) was not more positive than OH$^-$/$\bullet$OH potential (+2.4 V) [48]. Photogenerated holes cannot react with H_2O or OH$^-$ to generate $\bullet$OH. Therefore, the contribution of $\bullet$OH to PHP is not considered here. The generated $^1O_2$ may be converted from $\bullet O_2^-$. ($\bullet O_2^- + h^+ \rightarrow {}^1O_2$). To verify this, further ESR signal detection of $^1O_2$ was carried out in the presence of p-benzoquinone (PBQ, a sacrificial agent for $\bullet O_2^-$). As shown in Fig. 3c, the result shows that there is no signal of $^1O_2$ but only the signal of interaction between PBQ and 2,2,6,6-tetramethylpiperidine (TEMP, a sacrificial agent for $^1O_2$) [49], as the signal detected in the PBQ/TEMP system is consistent with the counterpart of NB-400/PBQ/TEMP. This suggests that the generated $^1O_2$ are converted from $\bullet O_2^-$.

Further, control experiments were performed. As shown in Fig. 3d, H_2O_2 cannot be produced under dark conditions, confirming the necessity of light irradiation for PHP. No H_2O_2 was produced in the presence of PBQ, indicating that the consumption of $\bullet O_2^-$ completely inhibits the H_2O_2 evolution. After adding TEMP, the yield of H_2O_2 decreased by 32% compared to the previous counterpart. It should be noted that after $^1O_2$ are consumed by TEMP, the conversion process of $\bullet O_2^-$ to $^1O_2$ is promoted, resulting in the reduction of $\bullet O_2^-$ and h^+. Meanwhile, the reduction of h^+ may lead to the promotion of the O_2 reduction process, leading to the increase of $\bullet O_2^-$ [15]. That is, the addition of $^1O_2$ sacrificial agent may cause the change of $\bullet O_2^-$, which further affects the yield of H_2O_2. Therefore, it is necessary to confirm the change of $\bullet O_2^-$ in the presence of TEMP. Nitro blue tetrazolium (NBT), a $\bullet O_2^-$ scavenger, can
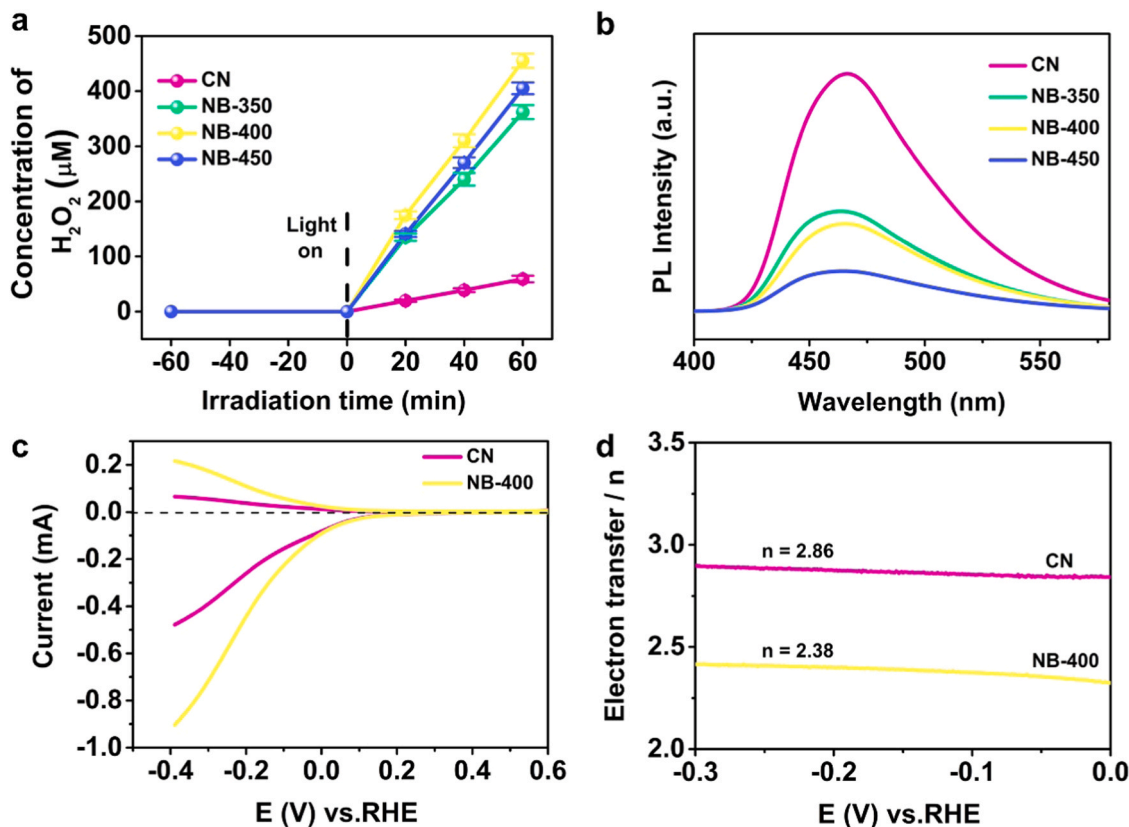

Fig. 3. (a) Photocatalytic H_2O_2 formation over different catalysts in 60 min under visible light irradiation ($\lambda > 420$ nm), respectively. (b) Photoluminescence (PL) spectra of CN and NB-x. (c) RRDE curves of CN and NB-400 measured at 1600 rpm in 0.10 M PBS. (d) Electron transfer numbers at different potentials calculated from RRDE data.
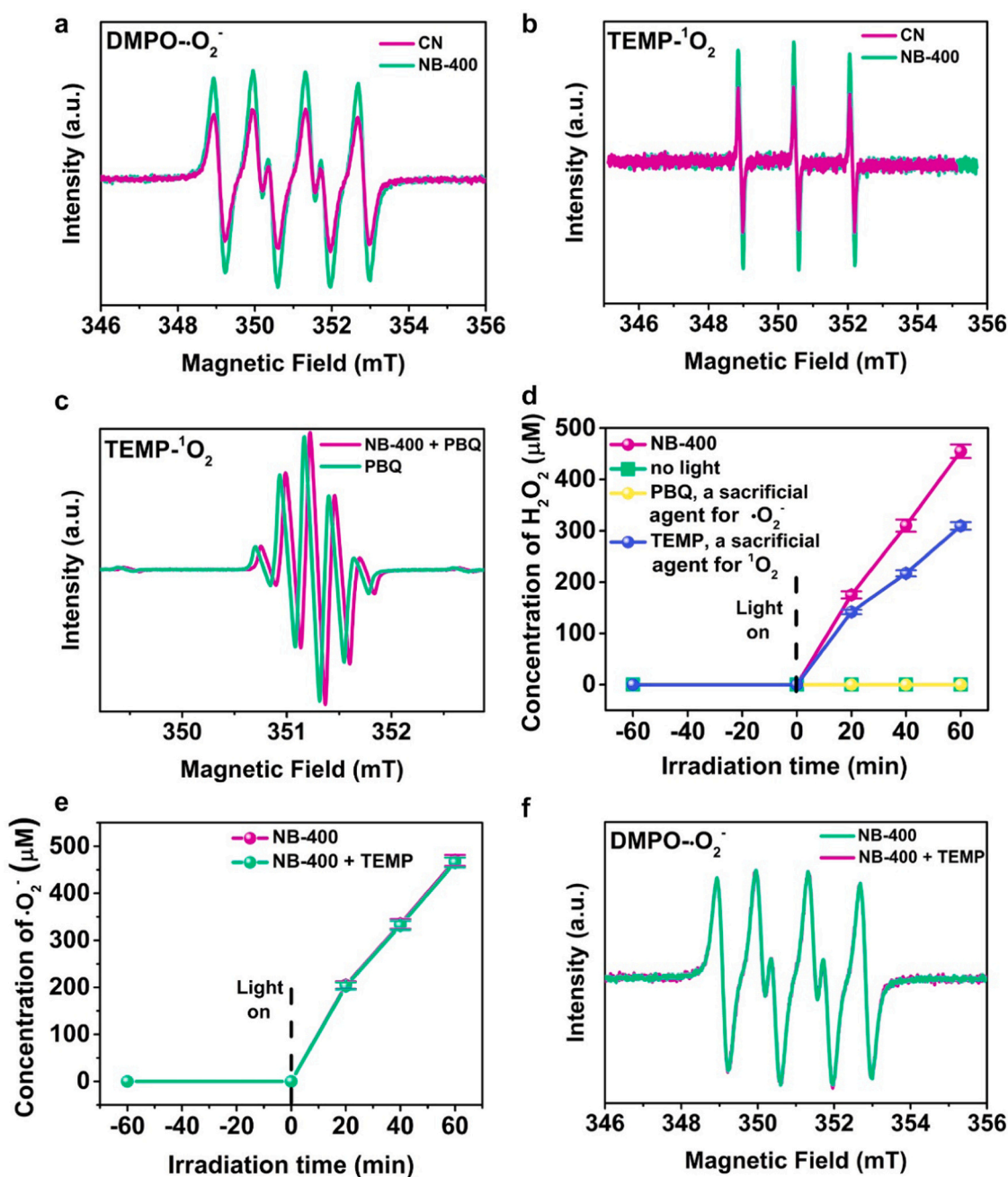
Fig. 4. ESR spectra of (a) DMPO-•O_2^- adduct and (b) TEMP-$^1O_2$ adduct for CN and NB-400 under visible-light illumination, respectively. (c) ESR spectra of TEMP-$^1O_2$ adduct after adding PBQ with and without NB-400. (d) Comparison of the photocatalytic H_2O_2 production under different conditions for NB-400. The concentration of sacrificial agent is 0.14 mM. (e) The effect of TEMP on •O_2^- formation during the photoreaction over NB-400. Reaction conditions: water (100 mL), NB-400 (0.10 g, 1 g L^{-1}), TEMP (0.14 mM), NBT (0.054 mM), $\lambda \geq 420$ nm, 25 °C. (f) ESR spectra of TEMP-•O_2^- adduct for NB-400 with and without TEMP under visible-light illumination.

be consumed by •O_2^- to determine the amount of •O_2^- produced [50]. As shown in Fig. 3e, after TEMP was added, the concentration of •O_2^- only dropped by ~1%. Moreover, the ESR signal intensity of •O_2^- over NB-400 remains unchanged with the addition of TEMP (Fig. 3f). These indicate that the addition of TEMP has almost no effect on •O_2^-. Combined with the scavenger experiment of $^1O_2$, it can be concluded that $^1O_2$ may be intermediate products in PHP. In general, a part of •O_2^- can be directly converted to H_2O_2 (•$O_2^- \rightarrow H_2O_2$), while the other part of •O_2^- is first converted to $^1O_2$ in the PHP process (•$O_2^- \rightarrow {}^1O_2 \rightarrow H_2O_2$). Superoxide radical anion plays a major role in the H_2O_2 production. A variety of ROS and their mutual conversion bring more reasonable possibilities for the H_2O_2 generation.

Based on the ESR data, the •O_2^- production of NBCN is only about 1.5 times that of CN, while the H_2O_2 production rate of NBCN is 7.7 times that of CN. This can be explained in two ways. First, after •O_2^- is generated, further reaction is needed to generate H_2O_2. The results of the RRDE experiment show that NBCN has a higher selectivity for PHP than CN, indicating that the conversion rate of •O_2^- to H_2O_2 on NBCN is higher. Second, in the actual reaction, NBCN can promote the conversion of a part of •O_2^- into $^1O_2$ (•$O_2^- + h^+ \rightarrow {}^1O_2$). In the ESR experiment, the generated •O_2^- was immediately captured by DMPO to generate DMPO-•O_2^- and could not be converted into $^1O_2$. Compared to CN, NBCN can more effectively promote the production of $^1O_2$. The generated $^1O_2$ can not only be effectively converted into H_2O_2, but also

consume additional h^+, which further promotes the O_2 reduction process for PHP and keep the amount of $\bullet O_2^-$ basically unchanged.

3.4. Analysis of electronic structure and active site

To explore the specific modification effects of NV and B doping on CN, theoretical calculations were performed. As shown in Fig. 5a, the result of density of states (DOS) shows that the generation of NV introduces defect states near the Fermi level. Interestingly, an intermediate band is generated at -2.13 eV. Since this intermediate band is introduced by doped B and the intensity of the corresponding DOS is large enough to contribute to light absorption, it is regarded as the CBM of NBCN [51]. The doped B moves both CBM and VBM down and reduces the bandgap from 2.60 to 2.32 eV, which is consistent with the experimental results of DRS and VB XPS. The downward shift of VBM can enhance the oxidizing ability of h^+, which may further promote the dissociation of PD and the generation of H^+.

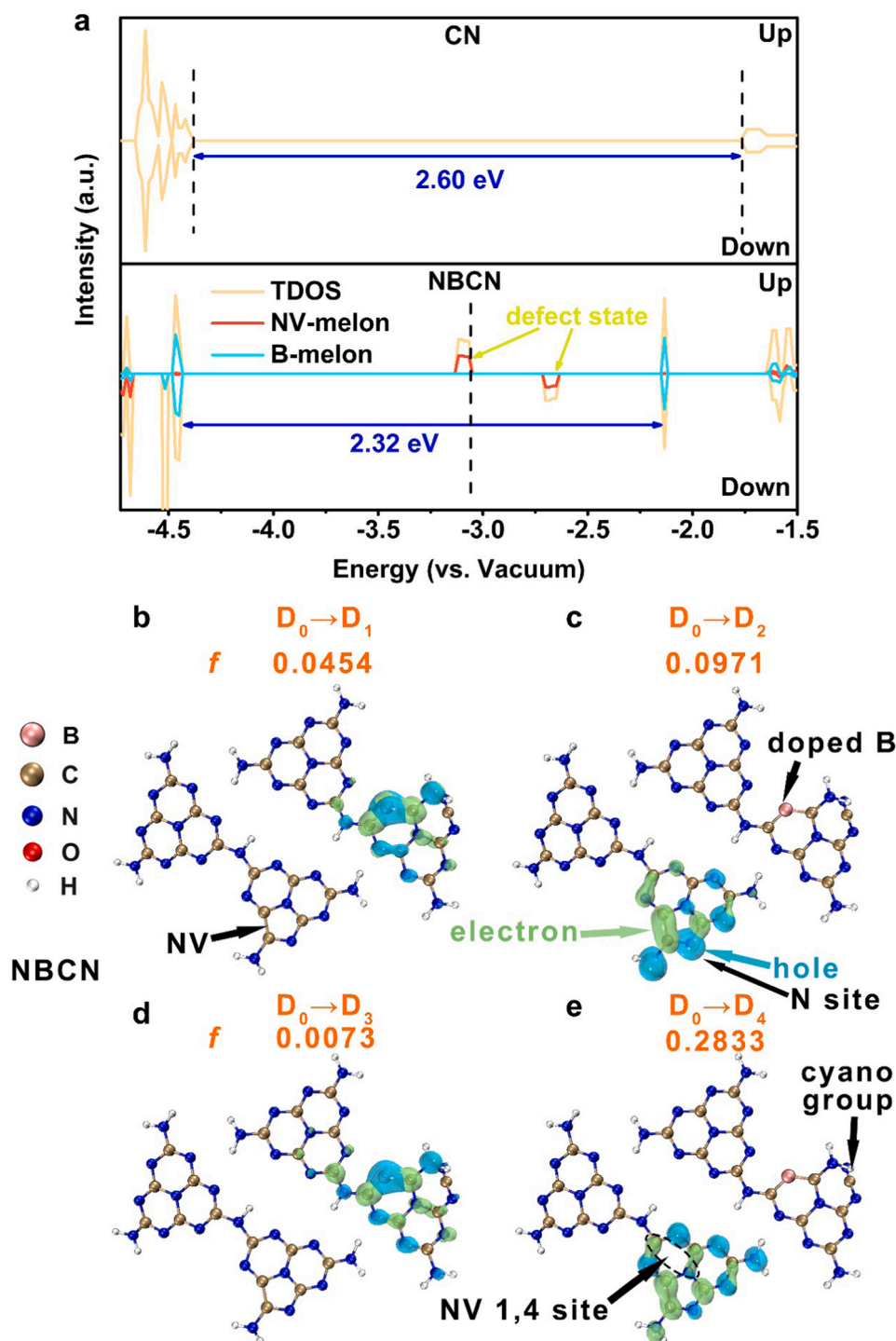The photocatalytic mechanism can be explored by DFT calculation,

Fig. 5. (a) Calculated DOS of pristine CN and NBCN, respectively. The black dotted line represents the Fermi level. The electron-hole distribution of NBCN for (b) $D_0 \rightarrow D_1$, (c) $D_0 \rightarrow D_2$, (d) $D_0 \rightarrow D_3$, and (e) $D_0 \rightarrow D_4$ excitations, respectively. f represents the value of oscillator strength. Green and blue isosurfaces represent electron and hole distributions, respectively. The isosurface value is 0.003 e/Å³.

such as band structure [42], charge density [14,42] and electrostatic potential [52]. Unfortunately, electronic excitation process is a transition from the ground state to excited state, rather than an occupied orbital to a non-occupied orbital [53]. To more accurately explore the complex light reaction process, such as probability of transition and electron-hole distribution, time-dependent density functional theory (TDDFT) calculations need to be performed. First, the distribution position of electron (e^-) and h^+ was confirmed by TDDFT calculation. It is worth mentioning that the $<S^{**}2>$ of investigated excited states are all close to the ideal value, indicating that the effect of spin contamination can be ignored (Table S1). As shown in Fig. 5, the oscillator strength **f** of $D_0 \rightarrow D_3$ excitation (0.0073) is less than 0.01 (Fig. 5d), indicating that the excitation is dark [53]. In contrast, the other three excitations are bright. For $D_0 \rightarrow D_1$ excitation, both e^- and h^+ gather on the B-doped melon. In the $D_0 \rightarrow D_2$ and $D_0 \rightarrow D_4$ excitations, e^- are concentrated on the NV site and 1,4 site of melon adjacent to NV (NV 1,4 site), and h^+ gather on the N atoms near the NV (N site). The reduction and oxidation sites of the NBCN were determined by the spatial distribution of e^- and h^+, respectively.

The generated ROS have vital effects on PHP, which is confirmed by control experiments and ESR characterization. To explore the specific activation of O_2 by the NBCN and the conversion between ROS, the electronic excitations of O_2 adsorbed on the above reduction sites were studied based on experimental results. When O_2 is adsorbed on the B site, a photogenerated electron can be transferred to O_2 to generate $\bullet O_2^-$ through $Q_0 \rightarrow Q_3$ or $Q_0 \rightarrow Q_4$ excitation ($e^- + O_2 \rightarrow \bullet O_2^-$, Fig. S10). Note

that the distance between $\bullet O_2^-$ and the h^+ left on NBCN surface is very close in this situation, which easily causes them to combine into $^1O_2$ ($\bullet O_2^- + h^+ \rightarrow {}^1O_2$). For the case where O_2 is adsorbed on the NV 1,4 site, O_2 can also obtain a photogenerated electron through $D_0 \rightarrow D_1$ excitation to generate $\bullet O_2^-$ (Fig. S11). It is worth noting that $\bullet O_2^-$ is relatively far away from the h^+ located on the NBCN surface, which may reduce the probability of charge recombination. Therefore, $\bullet O_2^-$ on the NV 1,4 site is more stable than that on the B site. On the other hand, the NV site cannot effectively activate the adsorbed O_2 as the corresponding $D_0 \rightarrow D_1$ and $D_0 \rightarrow D_2$ excitations are both dark (Fig. S12). In general, B site and NV 1,4 site may serve as charge recombination and reduction centers, promoting the generation of $^1O_2$ and $\bullet O_2^-$, respectively. Meanwhile, the B site and NV site that accumulate h^+ may be the active sites for the oxidation reaction.

Based on the above results, the reaction pathways of PHP were further explored through static DFT calculations. Twelve pathways were proposed.

3.5. Oxidation pathways dominated by h^+ of N site

As mentioned above, holes accumulate on N site (Fig. 5c,e), which may directly oxidize IPA to generate H^+ required for H_2O_2 generation. Here, oxidation pathways dominated by h^+ of N site were considered. In pathway (1), O_2 and IPA are initially located on the NV 1,4 site and the N site, respectively (Int-a in Fig. 6a). The methylene hydrogen (H1) of IPA can be transferred to the N site with a barrier of 0.91 eV (TS-1 in Fig. 6a).
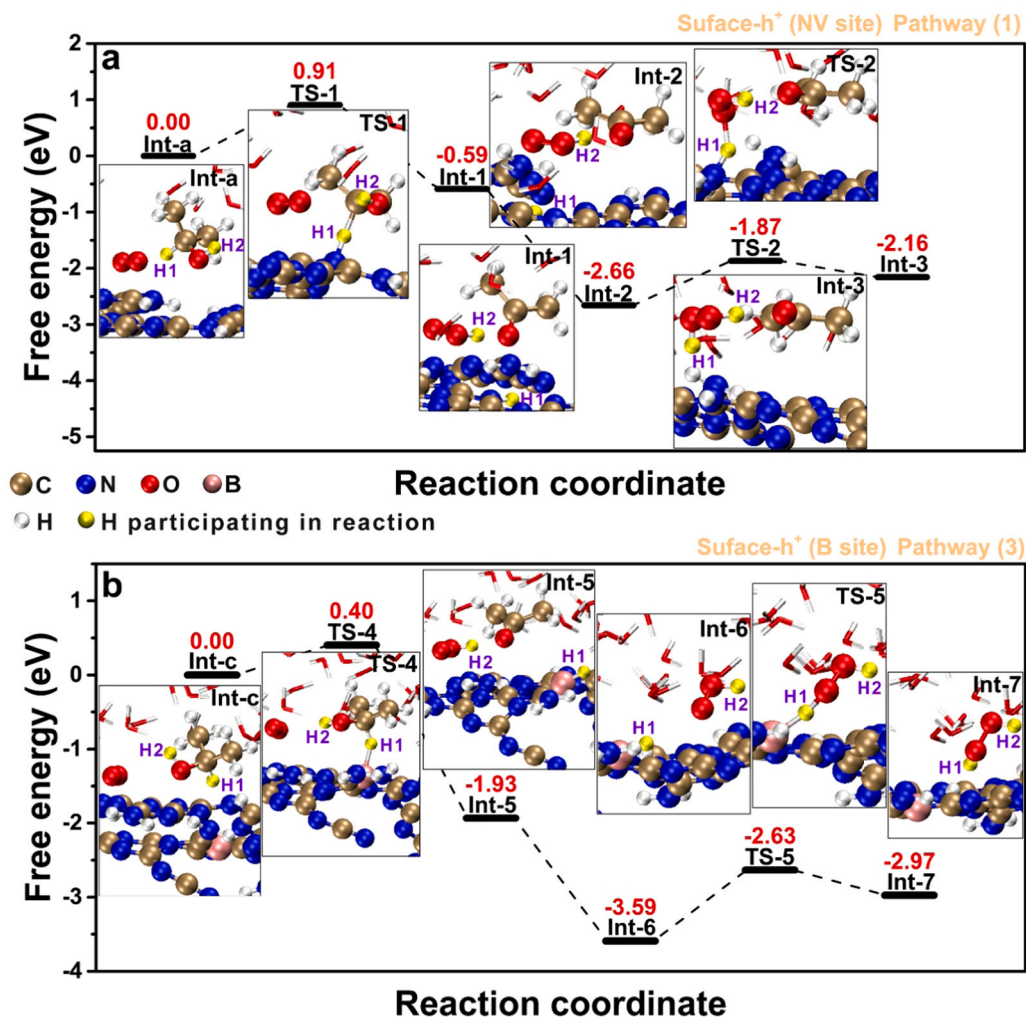

Fig. 6. Calculated reaction pathway for H_2O_2 generation dominated by h^+ of (a) N site and (b) B site, respectively.

Meanwhile, the photogenerated electron reduce O_2 to $\bullet O_2^-$. Subsequently, an electron on CH_3COHCH_3 transfers to the catalyst surface and further reduces $\bullet O_2^-$ to O_2^{2-}. Meanwhile, the hydroxyl hydrogen (H2) of CH_3COHCH_3 is converted to H^+ after donating an electron and combines with O_2^{2-} to form HO_2^- without energy barrier (Int-2 in Fig. 6a). That is, the current doubling effect induced by a photon. Finally, the OOH^- gradually approaches the H1 anchored on N site (Int-2 in Fig. 6a) and combines with it to generate H_2O_2, overcoming a reaction barrier of 0.79 eV (TS-2 and Int-3 in Fig. 6a). On the other hand, we also considered the case where the H1 of IPA moves to the NV site (pathway (2), Fig. S13a). Unfortunately, the corresponding energy barrier is as high as 1.4 eV, indicating the pathway (2) is difficult to occur.

3.6. Oxidation pathways dominated by h^+ of B site

The reaction pathways dominated by the h^+ of the B site were studied. As shown in pathway (3) of Fig. 6b, H1 of IPA can move to B site of NBCN and the corresponding reaction barrier is only 0.40 eV (TS-4), which is lower than the dissociation barrier of H1 (0.91 eV) in pathway (1). Then, OOH^- and H_2O_2 (Int-5 and Int −7 in Fig. 6b) are sequentially generated in the similar way as in pathway (1). However, OOH^- needs to overcome a reaction barrier as high as 0.96 eV to combine with H1 anchored on the B site (TS-5 in Fig. 6b). Although B site effectively reduces the barrier for H1 dissociation, it increases the barrier for combination of H1 and OOH^-, which is similar to the BEP relation in ammonia synthesis [12]. Due to the limitation of the BEP-like relation, the barrier of rate determining step (BRDS) of pathway (3) is higher than that of pathway (1). On the other hand, we also considered the case where the H1 anchored on the B site moves to the N atom adjacent to the

B site, but the corresponding barrier is as high as 1.94 eV (Fig. S13b). Thus, the corresponding pathway (4) is determined to be unfavorable.

3.7. Oxidation pathway dominated by ROS

As mentioned above, B site and NV 1,4 site can effectively activate O_2 to generate $^1O_2$ and $\bullet O_2^-$, respectively. In this section, the direct effect of ROS with oxidizing ability on IPA was considered. The $^1O_2$ adsorbed on the B site can directly obtain H1 and H2 of IPA to produce H_2O_2, overcoming a reaction barrier of 0.79 eV (pathway (5), Fig. 7a). It is worth mentioning that $^1O_2$ or $\bullet O_2^-$ can be easily confirmed by electronic structure analysis. Through the spin population analysis, it is found that the number of spin electrons of the O-O species of Int-d in pathway (5) is almost 0 (Fig. S15a), indicating that it is $^1O_2$. The $\bullet O_2^-$ located on the NV 1,4 site can also directly combine with H1 and H2 of IPA, experiencing a barrier of 0.62 eV (Fig. 7b). Similarly, it can be found that the number of spin electrons for the O-O species in Int-e is 1.00 (Fig. S15a), which confirms that it is $\bullet O_2^-$. In the following discussion, spin population analysis will continue to be used to confirm ROS. On the other hand, the ROS generated on the surface of the photocatalyst may diffuse into the solution and directly react with the IPA. As shown in Fig. 7c, $^1O_2$ on the B site can be desorbed from the catalyst surface to form free $^1O_2$ with a desorption energy of 0.12 eV (Int-11). Subsequently, free $^1O_2$ combines with H1 and H2 of IPA to generate H_2O_2 with a reaction barrier of 0.71 eV. Similarly, $\bullet O_2^-$ on the NV site can also undergo desorption and redox processes to generate H_2O_2, and the corresponding desorption energy and reaction barrier are 0.08 eV and 0.52 eV, respectively (pathway (8), Fig. 7d). It is worth noting that for pathway (8) dominated by free $\bullet O_2^-$, the whole reaction is endothermic.
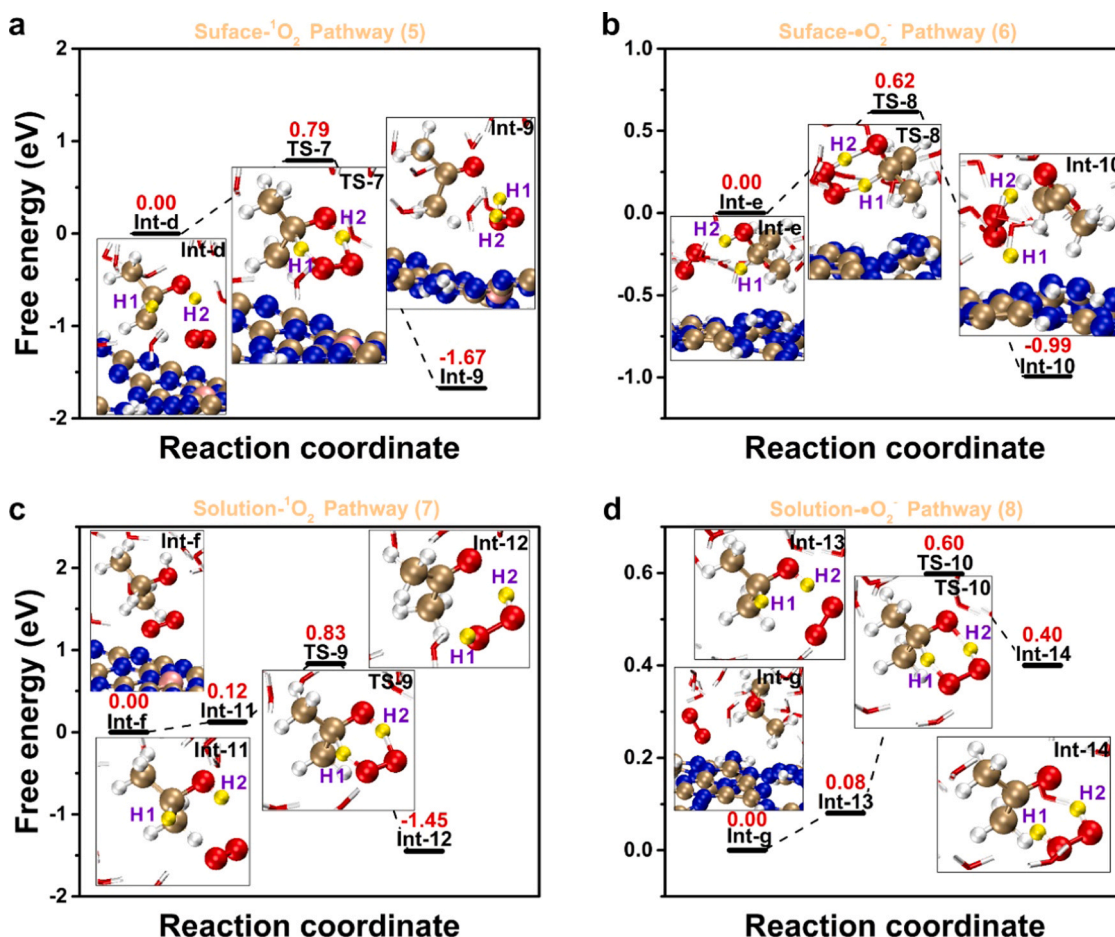

Fig. 7. Calculated reaction pathway for H_2O_2 generation dominated by (a) surface $^1O_2$, (b) surface $\bullet O_2^-$, (c) free $^1O_2$ and (d) free $\bullet O_2^-$, respectively.

3.8. Cooperation of ROS and water bridge

It is well known that water molecules in the solution can act as a bridge to transfer protons (water bridge) [36], which may promote the combination of protons and ROS to generate H_2O_2. The premise that ROS directly react with IPA is that they are sufficiently close. However, the reaction solution is mainly composed of water molecules, so that part of PD and IPA are also mainly surrounded by water molecules. Therefore, it is necessary to consider the synergy between ROS and adjacent water molecules in the PHP reaction. Here, the reaction pathways driven by surface or free ROS with the help of water bridge were studied. For surface $^1O_2$, we start with the situation where H1 and H2 of IPA point toward to $^1O_2$ and a water molecule adjacent to IPA ($H_2O_{(1)}$), respectively (Int-f in Fig. 8a). Subsequently, H1 and H2 moves to $^1O_2$ and $H_2O_{(1)}$, respectively. Meanwhile, another water molecule adjacent to $H_2O_{(1)}$ ($H_2O_{(2)}$) and $^1O_2$ obtain H3 of $H_2O_{(1)}$ and H4 of $H_2O_{(2)}$, respectively (Int-15 in Fig. 8). That is, H1 of IPA and H4 of $H_2O_{(2)}$ transfer to $^1O_2$ to generate H_2O_2. The two water molecules act as a bridge in this process, indirectly transferring the H2 of IPA to $^1O_2$. The entire reaction experiences a barrier of 0.67 eV (TS-11 in Fig. 8a). Similarly, surface $\bullet O_2^-$ (Fig. 8b), free $^1O_2$ (Fig. S14a) and free $\bullet O_2^-$ (Fig. S14b) can also cooperate with adjacent water molecules to oxidize IPA to generate H_2O_2, respectively. The corresponding barriers are 0.67, 0.92 and 0.68 eV, respectively.

The BRDS for 12 reaction pathways are shown in Fig. 8c. By comparing the value of BRDS, it can be seen that the pathways dominated by ROS are more favorable than the counterparts of h^+. The h^+ distributed in the NV site need to experience a relatively high energy

barrier (0.91 eV) to oxidize IPA, which can be attributed to the fact that the h^+ are located in the defect state with weak oxidizing ability (Fig. 5a). In contrast, although the h^+ accumulated in the B site with stronger oxidation ability can catalyze the dissociation of H1 with a lower barrier (0.40 eV), the desorption of H1 needs to overcome a larger barrier (0.96 eV). That is, the dissociation and desorption of H1 on NBCN surface is restricted by the BEP-like relation, resulting in a higher dissociation or desorption barrier. Among the four general pathways dominated by ROS, ROS can bypass the limitation of BEP-like relation and directly attack IPA to produce H_2O_2 with lower BRDS than those of the pathways dominated by h^+. Interestingly, the water bridge can promote the oxidation of IPA by $^1O_2$ on the B site and the subsequent H_2O_2 generation, and the corresponding BRDS is further reduced by 0.12 eV (pathway (9)) compared to the general pathway without water bridge assistance (pathway (5)). However, for the pathways dominated by surface $\bullet O_2^-$, free $^1O_2$ and free $\bullet O_2^-$, the water bridge cannot help to lower the reaction barrier. This suggests that the reduction of barrier in pathway (9) may be caused by the synergy of B site, $^1O_2$ and adjacent water molecules. To verify this, DOS analysis was performed on the TS-11 structure of pathway (9). As shown in Fig. S16, IPA, water bridge and B-doped melon all have relatively large DOS at −0.175 hartree, indicating that there are interactions between IPA and water bridge, as well as IPA and melon modified by B site (B-melon). In the same way, the DOS at −0.126 and −0.110 hartree also confirm the interactions between IPA and $^1O_2$, and $^1O_2$ and B-doped melon, respectively. The DOS analysis evidently demonstrates the strong synergistic effect between water bridge, $^1O_2$ and B site in producing H_2O_2, highlight the key role of B site due to its unique electronic structure. On the other hand, the BRDS

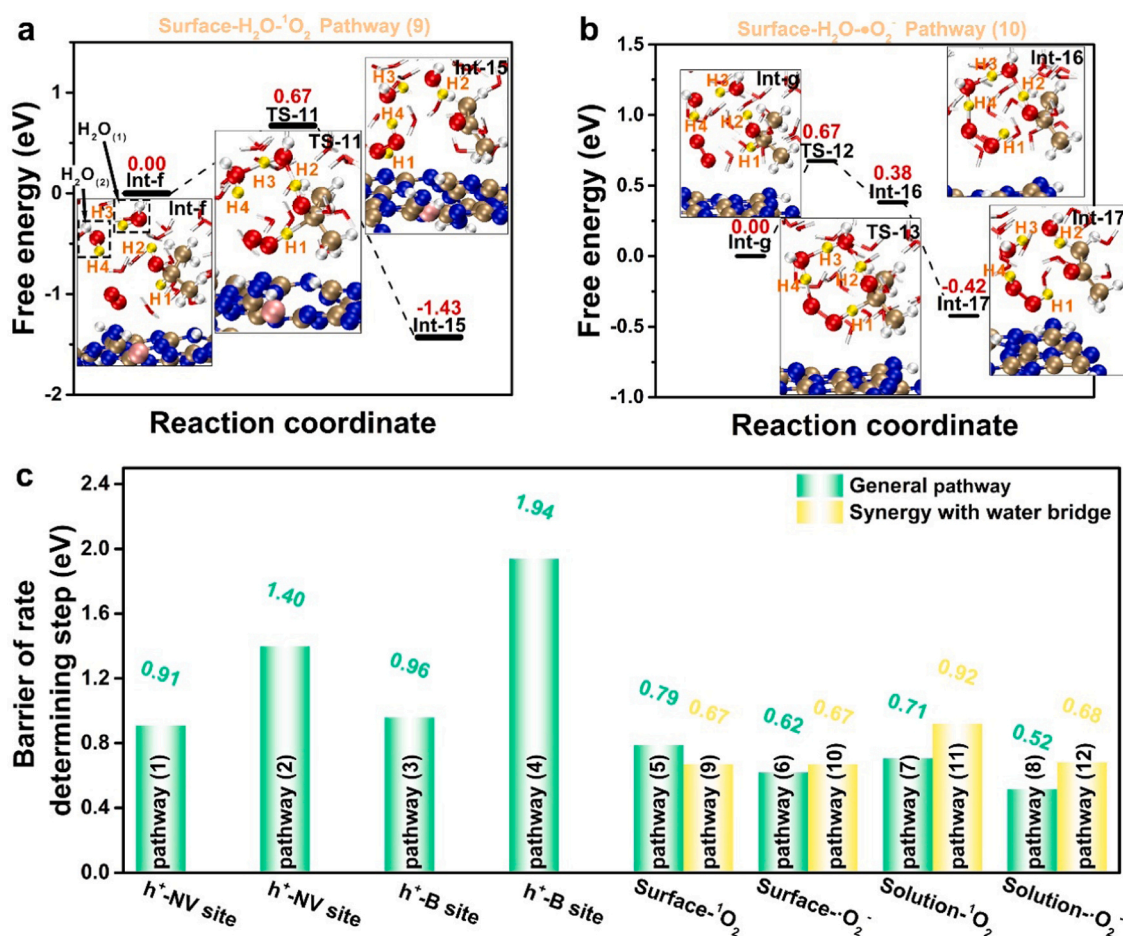**Fig. 8.** Calculated reaction pathway for H_2O_2 generation dominated by (a) surface $^1O_2$ and (b) surface $\bullet O_2^-$ with the assistance of water bridge. (c) BRDS for all calculated pathways.

of pathway (8) dominated by free $\bullet O_2^-$ is the lowest, but the whole reaction is endothermic. Nevertheless, the BRDS of pathway (6) dominated by the surface $\bullet O_2^-$ is lower than those of the other 10 pathways. This indicates that $\bullet O_2^-$ is the main active species in PHP, which is consistent with the results of the control experiments (Fig. 4).

The proposed reaction mechanisms are summarized in Table 1 and compared with reported studies. In the reported mechanisms, the generation pathway of H_2O_2 are relatively simple, with only one-step two-electron or two-step single-electron reduction of O_2, and h^+ is regarded as the only driving force for H^+ generation. In contrast, we considered the attack of surface or free ROS on PD with and without assistance of water bridge, and therefore discovered 8 additional reaction pathways. It is worth mentioning that PHP in pure water is indeed a green way to prepare H_2O_2, but the current level of photoactivity is too low to be meaningful as a sustainable method [2]. In contrast, PHP with the help of PD has been successfully applied to the disinfection of *Escherichia coli* [2]. Moreover, by choosing a more suitable PD, such as benzylamine, people can not only prepare H_2O_2, but also obtain value-added chemical [11]. Therefore, PHP with using PD has broad prospects. Although IPA is used as PD in this work, the proposed reaction mechanisms with ROS as the driving force of oxidation and the summarized BEP-like relation still have reference and guiding significance for related study.

4. Conclusion

CN materials co-modified by B doping and NV were prepared for PHP and corresponding reaction mechanism was systematically investigated. The H_2O_2 productive rate of NB-400 is 455 μM h^{-1}, which is 7.7 times higher than that of pristine CN. Holes can accumulate on N site and B site and induce the dissociation of H1 and H2 in IPA. However, the BEP-like relation limits the dissociation and desorption of H1 on N site and B site, respectively, resulting in relatively high BRDS. Interestingly, NV 1,4 site and B site can promote the production of $\bullet O_2^-$ and $^1O_2$, respectively. The generated $\bullet O_2^-$ and $^1O_2$ can directly attack IPA or diffuse into the solution to react with unabsorbed IPA to generate H_2O_2, and the corresponding BRDSs are lower than those of pathways dominated by h^+. Moreover, the $^1O_2$ generated on B site have a synergistic effect with the surrounding water molecules, further reducing the reaction barrier. The enhanced photocatalytic performance can be attributed to the appropriate electronic structure changed by modification sites, which promotes the generation of ROS. The resulting ROSs induce a variety of novel and more favorable pathways to produce H_2O_2, and the hole-dominated oxidation mechanism does not play a major role. This work developed an effective photocatalyst for PHP, expanding the existing mechanism by revealing the specific role of h^+ and ROS, which provides a favorable reference for highly selective two-electron photocatalytic H_2O_2 evolution.

CRediT authorship contribution statement

Jun Luo: Conceptualization, Methodology, Validation, Investigation, Writing – original draft, Writing – review & editing. **Changzheng Fan:** Conceptualization, Writing – review & editing, Supervision, Project administration, Funding acquisition. **Lin Tang:** Conceptualization, Writing – review & editing, Supervision, Project administration, Funding acquisition. **Yani Liu:** Writing – review & editing, Investigation. **Zhixuan Gong:** Writing – review & editing, Investigation. **Tangshan Wu:** Writing – review & editing, Investigation. **Xinlan Zhen:** Writing – review & editing, Investigation. **Chengyang Feng:** Writing – review & editing. **Haopeng Feng:** Writing – review & editing. **Lingling Wang:** Writing – review & editing. **Liang Xu:** Writing – review & editing. **Ming Yan:** Writing – review & editing.

Declaration of Competing Interest

The authors declare that they have no known competing financial

Table 1

Comparison of reaction mechanisms of the reported study and this work. $O_{2\,s}$, $\bullet O_2^-\,_s$ and $^1O_2\,_s$ represent O_2, $\bullet O_2^-$ and $^1O_2$ adsorbed on catalyst surface, respectively. $O_{2\,f}$, $\bullet O_2^-\,_f$ and $^1O_2\,_f$ represent free O_2, $\bullet O_2^-$ and $^1O_2$, respectively.

Reaction mechanism	Reported study [2,3,5,9,15, 54–57]	This work
The driving force of H^+ generation in PHP	Hole	Hole, $\bullet O_2^-$ and $^1O_2$
The specific role of O_2 in PHP	It is reduced by photogenerated electrons and then combined with the generated H^+ to form H_2O_2.	1. It is reduced by photogenerated electrons and then combined with the generated H^+ to form H_2O_2. 2. It can be converted into $\bullet O_2^-$ and $^1O_2$ on photocatalyst surface, which can directly or indirectly react with PD to generate H_2O_2. 3. It can be converted into $\bullet O_2^-$ and $^1O_2$ on photocatalyst surface and desorbed into solution, which can directly or indirectly react with PD to generate H_2O_2.
The reaction involved in PHP	1. $R\text{-}CH_2OH + 2h^+ \rightarrow R\text{-}CHO + 2H^+$ $O_2 + 2H^+ + 2e^- \rightarrow H_2O_2$ 2. $R\text{-}CH_2OH + 2h^+ \rightarrow R\text{-}CHO + 2H^+$ $O_2 + e^- \rightarrow \bullet O_2^-$ $\bullet O_2^- + e^- + 2H^+ \rightarrow H_2O_2$ 3. $R\text{-}CHOH\text{-}R + h^+ \rightarrow R\text{-}COH\text{-}R + H^+$ $O_2 + e^- \rightarrow \bullet O_2^-$ $R\text{-}COH\text{-}R \rightarrow R\text{-}CHO\text{-}R + e^- + H^+$ $\bullet O_2^- + e^- + 2H^+ \rightarrow H_2O_2$ 4. $R\text{-}CH_2OH + 2h^+ \rightarrow R\text{-}CHO + 2H^+$ $O_2 + e^- \rightarrow \bullet O_2^-$ $\bullet O_2^- + h^+ \rightarrow {}^1O_2$ $^1O_2 + 2H^+ + 2e^- \rightarrow H_2O_2$	1. $R\text{-}CHOH\text{-}R + h^+ \rightarrow R\text{-}COH\text{-}R + H^+$ $O_2 + e^- \rightarrow \bullet O_2^-$ $R\text{-}COH\text{-}R \rightarrow R\text{-}CHO\text{-}R + e^- + H+$ $\bullet O_2^- + e^- + 2H^+ \rightarrow H_2O_2$ 2. $O_{2\,s} + e^- \rightarrow \bullet O_2^-\,_s$ $\bullet O_2^-\,_s + R\text{-}CHOH\text{-}R \rightarrow H_2O_2 + R\text{-}COH\text{-}R + e^-$ 3. $O_{2s} + e^- \rightarrow \bullet O_2^-\,_s$ $\bullet O_2^-\,_s + h^+ \rightarrow {}^1O_2\,_s$ $^1O_{2s} + R\text{-}CHOH\text{-}R \rightarrow H_2O_2 + R\text{-}COH\text{-}R$ 4. $O_{2s} + e^- \rightarrow \bullet O_2^-\,_s$ $\bullet O_2^-\,_s \rightarrow \bullet O_2^-\,_f$ $\bullet O_2^-\,_f + R\text{-}CHOH\text{-}R \rightarrow H_2O_2 + R\text{-}COH\text{-}R + e^-$ 5. $O_{2s} + e^- \rightarrow \bullet O_2^-\,_s$ $\bullet O_2^-\,_s + h^+ \rightarrow {}^1O_2\,_s$ $^1O_{2s} \rightarrow {}^1O_2\,_f$ $^1O_{2f} + R\text{-}CHOH\text{-}R \rightarrow H_2O_2 + R\text{-}COH\text{-}R$ 6. $O_{2s} + e^- \rightarrow \bullet O_2^-\,_s$ $\bullet O_2^-\,_s + R\text{-}CHOH\text{-}R + H_2O_{(1)} + H_2O_{(2)} \rightarrow H_2O_2 + R\text{-}COH\text{-}R + H_2O_{(3)} + H_2O_{(4)} + e^-$ 7. $O_{2s} + e^- \rightarrow \bullet O_2^-\,_s$ $\bullet O_2^-\,_s + h^+ \rightarrow {}^1O_{2s}$ $^1O_{2s} + R\text{-}CHOH\text{-}R + H_2O_{(1)} + H_2O_{(2)} \rightarrow H_2O_2 + R\text{-}COH\text{-}R + H_2O_{(3)} + H_2O_{(4)}$ 8. $O_{2s} + e^- \rightarrow \bullet O_2^-\,_s$ $\bullet O_2^-\,_s \rightarrow \bullet O_2^-\,_f$ $\bullet O_2^-\,_f + R\text{-}CHOH\text{-}R + H_2O_{(1)} + H_2O_{(2)} \rightarrow H_2O_2 + R\text{-}COH\text{-}R + H_2O_{(3)} + H_2O_{(4)} + e^-$ 9. $O_{2s} + e^- \rightarrow \bullet O_2^-\,_s$ $\bullet O_2^-\,_s + h^+ \rightarrow {}^1O_2\,_s$ $^1O_{2s} \rightarrow {}^1O_{2f}$ $^1O_{2f} + R\text{-}CHOH\text{-}R + H_2O_{(1)} + H_2O_{(2)} \rightarrow H_2O_2 + R\text{-}COH\text{-}R + H_2O_{(3)} + H_2O_{(4)}$

interests or personal relationships that could have appeared to influence the work reported in this paper.

Appendix A. Supporting information

Supplementary data associated with this article can be found in the online version at doi:10.1016/j.apcatb.2021.120757.

References

[1] K. Mase, M. Yoneda, Y. Yamada, S. Fukuzumi, Seawater usable for production and consumption of hydrogen peroxide as a solar fuel, Nat. Commun. 7 (2016) 11470, https://doi.org/10.1038/ncomms11470.

[2] P. Zhang, Y. Tong, Y. Liu, J.J.M. Vequizo, H. Sun, C. Yang, A. Yamakata, F. Fan, W. Lin, X. Wang, W. Choi, Heteroatom dopants promote two-electron O2 reduction for photocatalytic production of H2O2 on polymeric carbon nitride, Angew. Chem. Int. Ed. 59 (2020) 16209–16217, https://doi.org/10.1002/anie.202006747.

[3] Y. Xie, Y. Li, Z. Huang, J. Zhang, X. Jia, X.-S. Wang, J. Ye, Two types of cooperative nitrogen vacancies in polymeric carbon nitride for efficient solar-driven H2O2 evolution, Appl. Catal. B: Environ. 265 (2020), 118581, https://doi.org/10.1016/j.apcatb.2019.118581.

[4] S. Li, G. Dong, R. Hailili, L. Yang, Y. Li, F. Wang, Y. Zeng, C. Wang, Effective photocatalytic H2O2 production under visible light irradiation at g-C3N4 modulated by carbon vacancies, Appl. Catal. B: Environ. 190 (2016) 26–35, https://doi.org/10.1016/j.apcatb.2016.03.004.

[5] Z. Zhu, H. Pan, M. Murugananthan, J. Gong, Y. Zhang, Visible light-driven photocatalytically active g-C3N4 material for enhanced generation of H2O2, Appl. Catal. B: Environ. 232 (2018) 19–25, https://doi.org/10.1016/j.apcatb.2018.03.035.

[6] Y. Shiraishi, Y. Kofuji, H. Sakamoto, S. Tanaka, S. Ichikawa, T. Hirai, Effects of surface defects on photocatalytic H2O2 production by mesoporous graphitic carbon nitride under visible light irradiation, ACS Catal. 5 (2015) 3058–3066, https://doi.org/10.1021/acscatal.5b00408.

[7] Y. Shiraishi, T. Takii, T. Hagi, S. Mori, Y. Kofuji, Y. Kitagawa, S. Tanaka, S. Ichikawa, T. Hirai, Resorcinol–formaldehyde resins as metal-free semiconductor photocatalysts for solar-to-hydrogen peroxide energy conversion, Nat. Mater. 18 (2019) 985–993, https://doi.org/10.1038/s41563-019-0398-0.

[8] Y. Kofuji, Y. Isobe, Y. Shiraishi, H. Sakamoto, S. Ichikawa, S. Tanaka, T. Hirai, Hydrogen peroxide production on a carbon nitride–boron nitride-reduced graphene oxide hybrid photocatalyst under visible light, Chemcatchem 10 (2018) 2070–2077, https://doi.org/10.1002/cctc.201701683.

[9] Z. Wei, M. Liu, Z. Zhang, W. Yao, H. Tan, Y. Zhu, Efficient visible-light-driven selective oxygen reduction to hydrogen peroxide by oxygen-enriched graphitic carbon nitride polymers, Energy Environ. Sci. 11 (2018) 2581–2589, https://doi.org/10.1039/c8ee01316k.

[10] Y. Shiraishi, S. Kanazawa, D. Tsukamoto, A. Shiro, Y. Sugano, T. Hirai, Selective hydrogen peroxide formation by titanium dioxide photocatalysis with benzylic alcohols and molecular oxygen in water, ACS Catal. 3 (2013) 2222–2227, https://doi.org/10.1021/cs400511q.

[11] Z. Tian, C. Han, Y. Zhao, W. Dai, X. Lian, Y. Wang, Y. Zheng, Y. Shi, X. Pan, Z. Huang, H. Li, W. Chen, Efficient photocatalytic hydrogen peroxide generation coupled with selective benzylamine oxidation over defective ZrS3 nanobelts, Nat. Commun. 12 (2021) 2039, https://doi.org/10.1038/s41467-021-22394-8.

[12] T. Bligaard, J.K. Nørskov, S. Dahl, J. Matthiesen, C.H. Christensen, J. Sehested, The Brønsted–Evans–Polanyi relation and the volcano curve in heterogeneous catalysis, J. Catal. 224 (2004) 206–217, https://doi.org/10.1016/j.jcat.2004.02.034.

[13] A. Vojvodic, A.J. Medford, F. Studt, F. Abild-Pedersen, T.S. Khan, T. Bligaard, J. K. Norskov, Exploring the limits: a low-pressure, low-temperature Haber–Bosch process, Chem. Phys. Lett. 598 (2014) 108–112, https://doi.org/10.1016/j.cplett.2014.03.003.

[14] D. Zhao, C.-L. Dong, W. Bin, C. Chen, Y.-C. Huang, Z. Diao, S. Li, L. Guo, S. Shen, Synergy of dopants and defects in graphitic carbon nitride with exceptionally modulated band structures for efficient photocatalytic oxygen evolution, Adv. Mater. 31 (2019) 1903545, https://doi.org/10.1002/adma.201903545.

[15] S. Zhao, X. Zhao, Insights into the role of singlet oxygen in the photocatalytic hydrogen peroxide production over polyoxometalates-derived metal oxides incorporated into graphitic carbon nitride framework, Appl. Catal. B: Environ. 250 (2019) 408–418, https://doi.org/10.1016/j.apcatb.2019.02.031.

[16] C. Kormann, D.W. Bahnemann, M.R. Hoffmann, Photocatalytic production of hydrogen peroxides and organic peroxides in aqueous suspensions of titanium dioxide, zinc oxide, and desert sand, Environ. Sci. Technol. 22 (1988) 798–806, https://doi.org/10.1021/es00172a009.

[17] J.P. Perdew, K. Burke, M. Ernzerhof, Generalized gradient approximation made simple, Phys. Rev. Lett. 77 (1996) 3865–3868, https://doi.org/10.1103/PhysRevLett.77.3865.

[18] S. Grimme, Semiempirical GGA-type density functional constructed with a long-range dispersion correction, J. Comput. Chem. 27 (2006) 1787–1799, https://doi.org/10.1002/jcc.20495.

[19] G. Kresse, J. Furthmüller, Efficiency of ab-initio total energy calculations for metals and semiconductors using a plane-wave basis set, Comput. Mater. Sci. 6 (1996) 15–50, https://doi.org/10.1016/0927-0256(96)00008-0.

[20] P.E. Blöchl, Projector augmented-wave method, Phys. Rev. B 50 (1994) 17953–17979, https://doi.org/10.1103/PhysRevB.50.17953.

[21] K. Mathew, R. Sundararaman, K. Letchworth-Weaver, T.A. Arias, R.G. Hennig, Implicit solvation model for density-functional study of nanocrystal surfaces and reaction pathways, J. Chem. Phys. 140 (2014), 084106, https://doi.org/10.1063/1.4865107.

[22] V. Wang, N. Xu, J. Liu, G. Tang, W. Geng, arXiv Prepr. arXiv 08269 (2019).

[23] J. Liu, Origin of high photocatalytic efficiency in monolayer g-C3N4/CdS heterostructure: a hybrid DFT study, J. Phys. Chem. C 119 (2015) 28417–28423, https://doi.org/10.1021/acs.jpcc.5b09092.

[24] G. He, J. Ma, H. He, Role of carbonaceous aerosols in catalyzing sulfate formation, ACS Catal. 8 (2018) 3825–3832, https://doi.org/10.1021/acscatal.7b04195.

[25] S. Grimme, J. Antony, S. Ehrlich, H. Krieg, A consistent and accurateab initioparametrization of density functional dispersion correction (DFT-D) for the 94 elements H-Pu, J. Chem. Phys. 132 (2010), 154104, https://doi.org/10.1063/1.3382344.

[26] Y. Zhao, D.G. Truhlar, The M06 suite of density functionals for main group thermochemistry, thermochemical kinetics, noncovalent interactions, excited states, and transition elements: two new functionals and systematic testing of four M06-class functionals and 12 other functionals, Theor. Chem. Acc. 120 (2008) 215–241, https://doi.org/10.1007/s00214-007-0310-x.

[27] R. Ditchfield, W.J. Hehre, J.A. Pople, Self-consistent molecular-orbital methods. IX. An extended gaussian-type basis for molecular-orbital studies of organic molecules, J. Chem. Phys. 54 (1971) 724–728, https://doi.org/10.1063/1.1674902.

[28] G.W. T.M. J. Frisch, H.B. Schlegel, G.E. Scuseria, M.A. Robb, J.R. Cheeseman, G. Scalmani, V. Barone, G.A. Petersson, H. Nakatsuji, X. Li, M. Caricato, A.V. Marenich, 2016.

[29] A.V. Marenich, C.J. Cramer, D.G. Truhlar, Universal solvation model based on solute electron density and on a continuum model of the solvent defined by the bulk dielectric constant and atomic surface tensions, J. Phys. Chem. B 113 (2009) 6378–6396, https://doi.org/10.1021/jp810292n.

[30] T. Lu, F. Chen, Multiwfn: a multifunctional wavefunction analyzer, J. Comput. Chem. 33 (2012) 580–592, https://doi.org/10.1002/jcc.22885.

[31] W. Humphrey, A. Dalke, K. Schulten, J. Mol. Graph. 14 (33–38) (1996) 27–38, https://doi.org/10.1016/0263-7855(96)00018-5.

[32] G. Henkelman, B.P. Uberuaga, H. Jónsson, A climbing image nudged elastic band method for finding saddle points and minimum energy paths, J. Chem. Phys. 113 (2000) 9901–9904, https://doi.org/10.1063/1.1329672.

[33] A. Heyden, A.T. Bell, F.J. Keil, Efficient methods for finding transition states in chemical reactions: comparison of improved dimer method and partitioned rational function optimization method, J. Chem. Phys. 123 (2005), 224101, https://doi.org/10.1063/1.2104507.

[34] J. VandeVondele, M. Krack, F. Mohamed, M. Parrinello, T. Chassaing, J. Hutter, Quickstep: fast and accurate density functional calculations using a mixed Gaussian and plane waves approach, Comput. Phys. Commun. 167 (2005) 103–128, https://doi.org/10.1016/j.cpc.2004.12.014.

[35] D. Wang, T. Sheng, J. Chen, H.-F. Wang, P. Hu, Identifying the key obstacle in photocatalytic oxygen evolution on rutile TiO2, Nat. Catal. 1 (2018) 291–299, https://doi.org/10.1038/s41929-018-0055-z.

[36] L. Wang, H. Xiao, T. Cheng, Y. Li, W.A. Goddard, Pb-activated amine-assisted photocatalytic hydrogen evolution reaction on organic-inorganic perovskites, J. Am. Chem. Soc. 140 (2018) 1994–1997, https://doi.org/10.1021/jacs.7b12028.

[37] S. Goedecker, M. Teter, J. Hutter, Separable dual-space Gaussian pseudopotentials, Phys. Rev. B 54 (1996) 1703–1710, https://doi.org/10.1103/PhysRevB.54.1703.

[38] C. Hartwigsen, S. Goedecker, J. Hutter, Relativistic separable dual-space Gaussian pseudopotentials from H to Rn, Phys. Rev. B 58 (1998) 3641–3662, https://doi.org/10.1103/PhysRevB.58.3641.

[39] J. VandeVondele, J. Hutter, Gaussian basis sets for accurate calculations on molecular systems in gas and condensed phases, J. Chem. Phys. 127 (2007), 114105, https://doi.org/10.1063/1.2770708.

[40] A. Thomas, A. Fischer, F. Goettmann, M. Antonietti, J.-O. Mueller, R. Schloegl, J. M. Carlsson, Graphitic carbon nitride materials: variation of structure and morphology and their use as metal-free catalysts, J. Mater. Chem. 18 (2008) 4893–4908, https://doi.org/10.1039/b800274f.

[41] Y. Cui, Z. Ding, X. Fu, X. Wang, Construction of conjugated carbon nitride nanoarchitectures in solution at low temperatures for photoredox catalysis, Angew. Chem. Int Ed. Engl. 51 (2012) 11814–11818, https://doi.org/10.1002/anie.201206534.

[42] H. Yu, R. Shi, Y. Zhao, T. Bian, Y. Zhao, C. Zhou, G.I.N. Waterhouse, L.-Z. Wu, C.-H. Tung, T. Zhang, Alkali-assisted synthesis of nitrogen deficient graphitic carbon nitride with tunable band structures for efficient visible-light-driven hydrogen evolution, Adv. Mater. 29 (2017), 1605148, https://doi.org/10.1002/adma.201605148.

[43] H. Gao, S. Yan, J. Wang, Y.A. Huang, P. Wang, Z. Li, Z. Zou, Towards efficient solar hydrogen production by intercalated carbon nitride photocatalyst, Phys. Chem. Chem. Phys. 15 (2013) 18077–18084, https://doi.org/10.1039/c3cp53774a.

[44] C. Feng, L. Tang, Y. Deng, J. Wang, Y. Liu, X. Ouyang, Z. Chen, H. Yang, J. Yu, J. Wang, Maintaining stable LSPR performance of W18O49 by protecting its oxygen vacancy: a novel strategy for achieving durable sunlight driven photocatalysis, Appl. Catal. B: Environ. 276 (2020), 119167, https://doi.org/10.1016/j.apcatb.2020.119167.

[45] Z. Hong, B. Shen, Y. Chen, B. Lin, B. Gao, Enhancement of photocatalytic H2 evolution over nitrogen-deficient graphitic carbon nitride, J. Mater. Chem. A 1 (2013) 11754–11761, https://doi.org/10.1039/C3TA12332D.

[46] G.-h Moon, M. Fujitsuka, S. Kim, T. Majima, X. Wang, W. Choi, Eco-friendly photochemical production of H2O2 through O2 reduction over carbon nitride

frameworks incorporated with multiple heteroelements, ACS Catal. 7 (2017) 2886–2895, https://doi.org/10.1021/acscatal.6b03334.

[47] H. Wang, Q. Lin, L. Yin, Y. Yang, Y. Qiu, C. Lu, H. Yang, Biomimetic design of hollow flower-like g-C3N4@PDA organic framework nanospheres for realizing an efficient photoreactivity, Small 15 (2019), 1900011, https://doi.org/10.1002/smll.201900011.

[48] Y. Deng, L. Tang, C. Feng, G. Zeng, Z. Chen, J. Wang, H. Feng, B. Peng, Y. Liu, Y. Zhou, Insight into the dual-channel charge-charrier transfer path for nonmetal plasmonic tungsten oxide based composites with boosted photocatalytic activity under full-spectrum light, Appl. Catal. B: Environ. 235 (2018) 225–237, https://doi.org/10.1016/j.apcatb.2018.04.075.

[49] J.T. Schneider, D.S. Firak, R.R. Ribeiro, P. Peralta-Zamora, Use of scavenger agents in heterogeneous photocatalysis: truths, half-truths, and misinterpretations, Phys. Chem. Chem. Phys. 22 (2020) 15723–15733, https://doi.org/10.1039/d0cp02411b.

[50] S. Obregón, Y. Zhang, G. Colón, Cascade charge separation mechanism by ternary heterostructured BiPO4/TiO2/g-C3N4 photocatalyst, Appl. Catal. B: Environ. 184 (2016) 96–103, https://doi.org/10.1016/j.apcatb.2015.11.027.

[51] W. Zhu, X. Qiu, V. Iancu, X.-Q. Chen, H. Pan, W. Wang, N.M. Dimitrijevic, T. Rajh, H.M. Meyer III, M.P. Paranthaman, G.M. Stocks, H.H. Weitering, B. Gu, G. Eres, Z. Zhang, Phys. Rev. Lett. 103 (2009), https://doi.org/10.1103/PhysRevLett.103.226401.

[52] L. Xu, Q. Li, X.-F. Li, M.-Q. Long, T. Chen, B. Peng, L.-L. Wang, Y. Yang, C. Shuai, Rationally designed 2D/2D SiC/g-C3N4photocatalysts for hydrogen production, Catal. Sci. Technol. 9 (2019) 3896–3906, https://doi.org/10.1039/c9cy00329k.

[53] C. Adamo, D. Jacquemin, The calculations of excited-state properties with Time-Dependent Density Functional Theory, Chem. Soc. Rev. 42 (2013) 845–856, https://doi.org/10.1039/c2cs35394f.

[54] Y. Shiraishi, S. Kanazawa, Y. Kofuji, H. Sakamoto, S. Ichikawa, S. Tanaka, T. Hirai, Sunlight-driven hydrogen peroxide production from water and molecular oxygen by metal-free photocatalysts, Angew. Chem. Int Ed. Engl. 53 (2014) 13454–13459, https://doi.org/10.1002/anie.201407938.

[55] C. Feng, L. Tang, Y. Deng, J. Wang, J. Luo, Y. Liu, X. Ouyang, H. Yang, J. Yu, J. Wang, Synthesis of leaf-vein-like g-C3N4 with tunable band structures and charge transfer properties for selective photocatalytic H2O2 evolution, Adv. Funct. Mater. 30 (2020), 2001922, https://doi.org/10.1002/adfm.202001922.

[56] S. Wu, H. Yu, S. Chen, X. Quan, Enhanced photocatalytic H2O2 production over carbon nitride by doping and defect engineering, ACS Catal. 10 (2020) 14380–14389, https://doi.org/10.1021/acscatal.0c03359.

[57] Y. Zhao, P. Zhang, Z. Yang, L. Li, J. Gao, S. Chen, T. Xie, C. Diao, S. Xi, B. Xiao, C. Hu, W. Choi, Mechanistic analysis of multiple processes controlling solar-driven H2O2 synthesis using engineered polymeric carbon nitride, Nat. Commun. 12 (2021) 3701, https://doi.org/10.1038/s41467-021-24048-1.